RSC Advances

PAPER

View Article Online
View Journal | View Issue

Cite this: *RSC Adv.*, 2026, **16**, 16474

Mg–Fe layered double hydroxides as multifunctional materials for manganese removal and methanol electrooxidation

Norhan Badawy,[a] Rehab Mahmoud,[bc] Amna A. Kotp,[d] Ahmed Farghali[d] and Amal Zaher*[a]

This study evaluated how well Mg–Fe layered double hydroxides (LDH) removed manganese (Mn^{2+}) from aqueous media and electrocatalytic methanol oxidation. The structural and physicochemical properties of the materials both prior to and after the adsorption process were characterized by X-ray diffraction, infrared analysis, particle size analysis, and field emission scanning electron microscopy. Adsorption was evaluated at different pH levels and adsorbent dosages, revealing that surface hydroxyl groups and interlayer anions are crucial for manganese uptake. The equilibrium data were well fitted by the Langmuir–Freundlich isotherm model, whereas the kinetic results followed those of the mixed 1,2-order and intraparticle diffusion models, indicating that monolayer adsorption was dominated by chemisorption mechanisms. Thermodynamic parameters confirmed that the adsorption process is spontaneous and exothermic, suggesting strong interactions between Mn^{2+} ions and the LDH surface through surface complexation and chemical bonding. The Mg–Fe LDH achieved a manganese removal efficiency exceeding 70%, and q_{max} was 198.99 mg g^{-1}. Furthermore, electrochemical studies demonstrated that both pristine LDH and Mn-loaded LDH (LDH/Mn) exhibit enhanced electrocatalytic activity toward methanol oxidation. The improved LDH/Mn performance was attributed to a larger electroactive surface area and improved charge-transfer kinetics. These results highlight the dual functionality of Mg–Fe LDH for environmental remediation and electrochemical energy conversion applications.

Received 29th January 2026
Accepted 12th March 2026

DOI: 10.1039/d6ra00805d

rsc.li/rsc-advances

1 Introduction

World population growth is a major challenge and is considered among the most serious issues affecting nearly every aspect of life, including water policy. Groundwater and other resources must be utilized to avoid chemical and microbiological contamination.[1]

The potential toxicity of heavy metals to both the environment and humans makes their poisoning of groundwater a major ecological issue.

Through the food supply chain, they can bioaccumulate and are not biodegradable.[2,3] Domestic sewage leakage from septic tanks is among the most important sources of groundwater pollution, leading to the spread of gastrointestinal diseases.[4]

Owing to increasing anthropogenic activities, manganese has been detected in both groundwater and surface water at varying concentrations.[5,6]

However, the human body needs certain amounts of essential minerals, which are thought to be cofactors for many different enzymes involved in intracellular function. Fortunately, manganese toxicity, which disrupts the central nervous system, can result from the consumption of this mineral in excess.[7,8] High levels of manganese in water systems result in the formation of oxide layers in pipelines with corrosion, which affects water quality. Compared with children who were exposed to controlled manganese, children who ingested 240–350 μg L^{-1} of manganese in water had reduced speed, manual dexterity, visual recognition and short-term memory.

There are various methods to remove metals from wastewater and water, including membrane filtration, adsorption, and ion exchange. These methods have been recently developed and reviewed.

Because of their great efficiency, affordability, and simplicity of use, adsorptions are regarded as among the most appropriate techniques.[9,10] Various water treatment residuals are employed to remove heavy metals through adsorption. Adsorption on a variety of substances, including biomaterials, clay minerals, and activated carbon, is the most efficient method for reducing metals.[11,12]

[a]*Environmental Science and Industrial Development Department, Faculty of Postgraduate Studies for Advanced Sciences, Beni-Suef University, Beni-Suef 62511, Egypt. E-mail: amal_z@psas.bsu.edu.eg; amal_2006z@yahoo.com*

[b]*Chemistry Department, Faculty of Science, Beni-Suef University, Beni-Suef 62511, Egypt*

[c]*Department of Chemistry, Faculty of Science, Chulalongkorn University, Bangkok 10330, Thailand*

[d]*Materials Science and Nanotechnology Department, Faculty of Postgraduate Studies for Advanced Sciences, Beni-Suef University, Egypt*

Layered double hydroxides (LDHs) are the best heavy metal adsorbents.[13] Layered double hydroxides (LDHs) play a vital role as effective adsorbents or photocatalysts in the remediation of water pollutants.[14–16] A type of artificial clay known as LDH has cationic layers that resemble brucite [$Mg(OH)_2$] and contain anions in the hydrated interlayer to maintain charge balance.

$[(MII)_{1-x}(MIII)_x(OH)_2]^{x+}(A^{m-}{}_{x/m})\cdot nH_2O$ is a general formula of LDHs.[17–19] Two-dimensional layered nano materials belong to the anionic clay family. Additionally, layered nanostructured LDH is a host-guest material made up of water molecules and positively charged metallic hydroxide plates with intercalated anions acting as guests.[20]

Studies employing LDHs to extract contaminants from aqueous solutions have increased in frequency in recent years.[21,22] The adsorption of heavy metals in wastewater has been the subject of several studies.[15]

However, simply discovering a viable nanoadsorbent is not enough to produce a large-scale adsorption approach that is both inexpensive and sustainable. Further investigations are needed to modify and employ waste adsorbents that are no longer regenerable to meet the tenets of the circular economy.[23,24] Reusing used adsorbents has become a crucial field of study in the modern era. Recently, many examples of different ways to recycle spent adsorbents have been reported.[25] Repurposing spent adsorbents into other applications and/or technologies, such as composite fillers, catalysis, supercapacitors and (bio)sensors, is one method of valorizing them. The use of adsorbents in the electro-oxidation of methanol is promising. Methanol is an oxidizable and feasible fuel for direct methanol fuel cells that generate water and carbon dioxide as byproducts of the oxidation process.[26] Methanol and water are used to generate carbon dioxide, protons, and electrons at the anode, and the external circuit is used by the electrons to move and decrease oxygen by reaching the cathode. An inventive field of research that could yield effective and reasonably priced anode materials is the investigation of waste adsorbents as methanol fuel cell anodes. In the future, direct alcohol fuel cells may function better and cost less as a result. Preparing, characterizing, and exploring multifunctional Mg–Fe LDH as a 2D nanoadsorbent for the adsorption of manganese (Mn) and using spent adsorbents as electrocatalysts are the goals of the current work. This work's main innovation is the creative repurposing of Mn-loaded waste adsorbents as effective electrocatalysts, which combines energy conversion applications with wastewater cleanup. Specifically, layered double hydroxides (LDHs) have a unique multifunctional property that allows high-capacity Mn species to be adsorbed as well as post-saturation catalytic activity. Through surface complexation, and interlayer incorporation mechanisms, LDHs exhibit a high affinity for Mn^{2+} ions because of their adjustable metal composition, high surface area, and abundance of hydroxyl groups. The added Mn species can behave as electroactive centers following adsorption, converting the wasted adsorbent from secondary waste to a valuable catalytic material. This dual use greatly improves material sustainability and aligns with circular economy principles. This method offers an environmentally friendly way to fabricate catalysts while lowering the disposal expenses related to depleted adsorbents. Previous studies have highlighted the adsorption efficiency of LDHs for heavy metals,[27,28] whereas recent reports have demonstrated their promising electrocatalytic behavior in water splitting applications.[29] Nevertheless, research on the direct conversion of waste adsorbents loaded with Mn into useful electrocatalysts is lacking. Consequently, the uniqueness and technological significance of the current findings are highlighted by specifically highlighting this integrated adsorption–electrocatalysis process. In addition to optimizing resource use, this strategy promotes sustainable material design for energy and environmental applications.

Additionally, various factors affect the process of disposing of manganese from contaminated water, including the solution pH, adsorbent dosage, manganese concentration, temperature, contact time, adsorption isotherm and kinetics of the process.[30] Finally, another application of the used adsorbent was as an electrocatalyst for DMEO.

A comparative study of different adsorbents for Mn^{2+}-polluted water and a comparison of the performance of the catalyst with recently published studies are shown in Tables 1 and 2, respectively.

2 Materials and methods

2.1. Materials

All pure chemicals were purchased from Merck (Germany) and included magnesium nitrate hexahydrate ($Mg(NO_3)\cdot 6H_2O$), ferric nitrate ($Fe(NO_3)_3\cdot 9H_2O$), manganese nitrate tetrahydrate ($Mn(NO_3)_2\cdot 4H_2O$), sodium bisulphite, sodium hydroxide (NaOH), HCL conc. 5.0 wt% Nafion solution; isopropanol, Methanol, and Alpha Aesar supplied a 1.0 mm thick graphite sheet (98% purity).

2.2. Preparation of Mg-layer double hydroxides (LDH)

Magnesium nitrate hexahydrate and ferric nitrate were weighed at a magnesium : iron ratio of 3 : 1 M, respectively. A solution was prepared in 100 mL of deionized water. In a 250 mL beaker, 1 N of sodium hydroxide was added until it reached pH = 9, with the addition rate being modified over a 24-hour aging period at 60 °C while vigorously stirring at 600 rpm. Finally, the precipitate was washed in a centrifuge for 20 minutes with distilled water until the pH of the filtrate reached 7 to ensure that the sodium ions were removed. The precipitate was placed in a crucible and dried at 70 °C overnight, after which it was ground manually.

2.3. Characterization of Mg-LDH

For the prepared Mg-LDH, three primary analytical methods are provided below. The FESEM JEOL JSM 5400LV instrument (Japan) was used to study the surface morphologies of the generated samples with scanning electron microscopy (SEM). The microstructure of the adsorbent was examined by high-resolution transmission electron microscopy (HRTEM, JEOL-JEM 100CX11, USA). X-ray diffraction (XRD) was performed (Shimadzu, Kyoto, Japan).

Table 1 Comparative study of different adsorbents

Adsorbents	Time (min)	Dose of adsorbent (g L^{-1})	Mn (mg L^{-1})	Temperature	pH	Adsorption capacity (mg g^{-1})	Ref.
Mg/Zn/Al LDH	75	0.25	80	45 °C	6	24.5	31
Co/Mo LDH	60	0.2	145	45 °C	5	36.95	32
Mg/Al LDH	60	0.3	>44.4	60 °C	9.5	192.6	33
Mg/Al/Ni LDH	60	0.3	100	45 °C	7	35.97	34
GO/ZNO nano composites	1080	0.02	28.4	22 °C	4 : 5	165.5	35
Mg–Fe LDH	120	0.6	100	25 °C	7	198.99	Present study

Table 2 Comparison of the performance of the catalyst with that in recently published studies

Adsorbents	Pollutants	Pollutants concentration	Time (h)	Dose of adsorbents (g L^{-1})	pH	Temp.	Adsorption capacity (mg g^{-1})	Ref.
Mg/Al-LDH	Po_4	10	4.16	0.005	3	25 °C	110	36
	No_3						45.5	
Mg/Fe-LDH/BIOCHAR	P	20	1	2	2–4	25 °C	17.46	37
Mg/Fe-LDH	Cd	20	2	100	5	25 °C	35	38
Mg/Fe-LDH – RHA 200	Pb	50	24	1	5–7	25 °C	17	39
	Cu^{2+}						23	
Mg/Fe-LDH@BB	Pb	Pb (500–1400)	6	1	6	25 °C	Pb 1112.6	40
	Cd	Cd (100–1000)					Cd 869.6	
	Zn	Zn (100–1000)					Zn 414.9	
Fe/MgLDH @nHAP	U(6)	(500–1400)	0.5	0.2	6	25 °C	845.16	41
Mg–Fe LDH	Mn	100	2	0.6	7	25 °C	198.99	This study

The speed of scanning was 8_in 20 min_1 over the angle of the diffraction range. An ATI Mattson Genesis series (KBr disk technique) apparatus (Model 960 M009 series) was used to record Fourier transfer infrared (FT-IR) spectra. Zeta potential was investigated by a Nano-Zeta sizer (Malvern Instruments Ltd, United Kingdom). The BET specific pore volume, specific surface area and pore size distribution of the nanoadsorbents were determined by N_2 adsorption with an automatic surface analyzer (TriStar II 3020; Micrometrics, USA). A mass spectrometer (ICP–MS Japan) was used to estimate the concentration of the manganese solution.

2.4. Adsorption study

To perform the experimental work, using a typical fluid solution, we conducted batch research in an operational system at ambient temperature. A manganese stock concentration of 100 ppm was used to obtain the optimal calibration curve (5–100 ppm) by creating a series of diluted concentrations.

First, six 250-mL beakers were created by adding 0.06 g of the synthesized catalyst (Mg–Fe LDH) and 100 mL of 5 ppm manganese stock solution, after which 0.2 N HCl and NaOH were added to the five beakers to decrease their pH to 3, 4, 6, 7, 9, and 11 *via* a pH meter (HACH). The five beakers were stirred for two hours on a magnetic stirrer. They were then measured after being filtered with a Bochner filter. An ICP spectrometer was used to determine the residual concentration of the manganese solution.

The quantity of manganese adsorbed per gram of Mg–Fe LDH (q_e) was calculated by the equations listed below:

$$q_e = \frac{(C_0 - C_e) \times V}{m} \quad (1)$$

$$\text{Removal percentage} = \frac{C_0 - C_e}{C_0} \times 100 \quad (2)$$

where q_e denotes the amount of manganese adsorbed in grams per liter, C_0 is the initial concentration of the manganese solution, and C_t is the manganese concentration in mg L^{-1} after adsorption at 120 minutes. W is the amount of LDH expressed in grams, and V is the volume of the manganese solution.

The previous experiment was repeated on five samples, after which the pH was adjusted to 7 and the adsorbent concentration was varied from 0.2 to 0.8 g L^{-1} for 2 hours. An ICP spectrometer was used to determine the amount of residual manganese solution. Additionally, we studied the effects of concentration, time and thermodynamics.

2.5. Use of spent Mg–Fe LDH in electrochemical methanol oxidation

Following adsorption, the wasted LDH powder was gathered, cleaned, and dried at 80 °C for 24 hours. Preparing the ink solution, a typical 2.0 mg of Mg–Fe LDH/Mn or Mg–Fe LDH sample was dispersed in 200 μL of isopropanol/D. W. mixed solvent with a ratio of 1 : 2, which contained 10 μL of Nafion solution (5.0 wt%). The mixture was sonicated for a minimum of 15 minutes to create a uniform ink. Afterward, 100 μL of the ink solution was put onto a 1 × 1 cm^2 piece of flexible graphite paper (thickness: 1 mm) and dried at 40 °C. Using a potentiostat/galvanostat (AUTOLAB PGSTAT 302 N, Metrohm, Herisau,

Switzerland) and NOVA 1.11 software, the electrocatalytic efficiency of LDH and LDH/Mn was assessed. Cyclic voltammetry (CV) and CA chronoamperometry were used, with a platinum sheet serving as the counter electrode and the reference electrode being Ag/AgCl in a three-electrode system. A 0.5 M NaOH electrolyte solution with and without methanol was used to assess the electrocatalytic performance of the generated electrodes. Scanning rates ranging from 5 to 100 mV s^{-1} were employed. The duration of the chronoamperometry (CA) experiments at 0.6 V was 1 h and 12 h.

2.6. Electrochemical procedures

For the voltammetric investigations, a potentiostat/galvanostat (AUTOLAB PGSTAT 302 N, Metrohm, Utrecht, Netherlands) was employed. It was connected to a three-electrode system that contained an $Ag/AgCl_3$ M KCl reference electrode, a Pt disc as the counter electrode, and an active electrode based on a graphite carbon sheet. Prior to conducting the electrochemical experiments, ten voltammetric cyclic scans with a scan rate of 100 mV s^{-1} were performed to activate the modified electrodes in phthalic acid. The scans ranged from 0.0 to 0.1 V. Cyclic voltammetry (CV), linear sweep voltammetry (LSV), and differential pulse voltammetry (DPV) were used for quantitative analysis, assay optimization, and characterization. NaOH was used as a support electrolyte in a 30 mL electrochemical cell; the measurements were carried out. To gather the metal ions surrounding the interface of the electrode, the modified CPE was immersed in an electrolyte solution for 30 seconds. Calibration curves were created using the standard addition approach.

3 Results and discussion

3.1. Characterization of the Mg–Fe LDH

3.1.1. X-ray diffraction. The XRD patterns of the generated materials and the typical XRD patterns of the LDH materials that resemble hydrotalcite were significantly similar (Fig. 1(a and b)).[42,43] The sharpness of the diffraction peaks in the synthesized Mg–Fe LDH XRD pattern verified its high crystallinity. Both the synthesized hydrotalcite-like compound and the native Mg–Fe LDH diffraction peaks matched the number on the ICDD card (00-058-0178). The structure of the Mg–Fe LDH, as depicted in (Fig. 1(a and b)) was confirmed by the characteristic reflections of layered double hydroxide. With the other peaks for the (012), (015), (018), (110), and (113) planes at high 2θ angles and the basal planes of the (003) and (006) planes at low 2θ angles.[44] The XRD results were compared prior to manganese adsorption.

The lattice parameters of Mg–Fe LDH were determined from X-ray diffraction data. The lattice parameter a is related to the average cation–cation distance within the layers of the prepared material.[45] The lattice parameter c is related to the thickness of one layer plus the interlayer spacing. The calculated a value of the prepared LDH was 3.06 Å, and the c value was 23.20 Å. The calculated lattice parameters confirm the formation of the characteristic layered structure of Mg–Fe LDH. After the

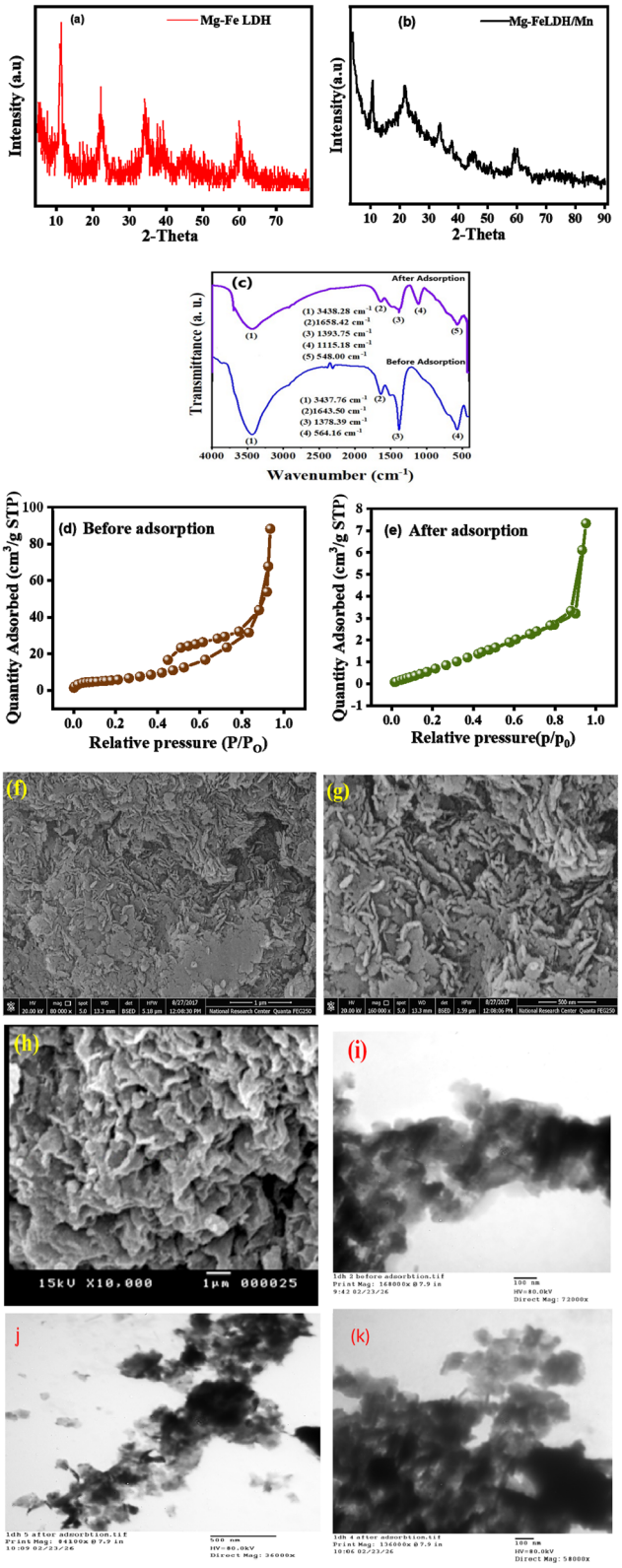

Fig. 1 Characterization of LDH (XRD (a and b) FTIR (c) N_2 adsorption–desorption isotherms and pore size distribution (d and e)) before and after adsorption–SEM (f–h) and TEM (i–k).

adsorption of Mn^{2+} onto Mg–Fe LDH, the lattice parameter remained almost unchanged, whereas the parameter *c* changed slightly to 23.21 Å. Adsorption through the interlayer type or on the surface did not significantly affect it.

Mn^{2+} is intercalated into the interlayer space, and the *c* value increases slightly because of expansion of the spacing. However, when the adsorption happened through surface of the layers by complexation or by chemical interaction, the *c* parameter only slightly changes.[46]

3.1.2. Fourier transform infrared spectroscopy. As illustrated in Fig. 1(c), FT-IR spectra of the materials were obtained. The impact of the IR spectra on the prepared adsorbent material (Mg–Fe LDH) before it was used to adsorb manganese ions from wastewater is shown in Fig. 1(c). IR spectral analysis revealed many peaks for different functional groups; the sharp stretching peak at 3437.73 cm^{-1} is ascribed to the stretching vibrations of the hydroxyl groups located in the LDH layers as well as interlayer water molecules and surface.

The sharp peak at 1643.5 cm^{-1} indicated weaker band formation because of the way that water molecules bend. On the basis of the data provided by,[47] the presence of an interlayer of MgO can be demonstrated by the asymmetric stretching absorption band of MgO close to 1382 cm^{-1}, suggesting the effective synthesis of Mg–Fe-LDH. The band at approximately 564.16 cm^{-1} is attributed to M–O–H and O–M–O lattice vibrations (when M = Mg and Fe).[48,49]

The effect of the IR spectrum on the prepared adsorbent material (Mg–Fe LDH) after the adsorption of Mn ions from wastewater is shown in Fig. 1(c). The slight appearance of a strong and powerful peak at 3700 cm^{-1} is because of the presence of the –OH group in $Mg(OH)_2$, which formed by a chemisorption process when the MgO was exposed to wastewater; thus, this peak did not appear in the calcined sample (Fig. 1(c)).

A new band after absorption at 1170 cm^{-1} matches the O–H bending vibrations joined with Mn atoms; this result matched that reported previously.[50] The deformation of the broad absorption band at 1653 cm^{-1} is the result of the presence of absorbed water molecules among the MnO_2 structure. The hydrated properties of MnO_2 might increase cation diffusion, thereby increasing the capacitance of MnO_2, and these findings matched those published by.[50] The deformation occurring at the band at approximately 584 cm^{-1} is attributed to the presence of Mn adsorbed on the LDH surface.

3.1.3. Morphology and surface study (FESEM, HRTEM, and surface area). The material morphology and shape after preparation could be estimated by FESEM and HRTEM. The Mg–Fe LDH produced by coprecipitation is displayed in Fig. 1(g–j).

SEM micrographs of Mg–Fe LDH reveal a characteristic plate-like layered morphology, which is typical for hydrotalcite-like materials, as shown in Fig. 1(f–g). The surface morphology appears as a sheet-like structure arranged in a hierarchical structure, forming a porous surface. These sheets appear randomly oriented and partially stacked, which produces a flower-like shape. The image also shows a rough surface texture and interparticle voids, indicating the presence of mesoporous spaces between the aggregated sheets. These pores facilitate the mass transfer and diffusion of Mn ions, which is beneficial for adsorption and catalytic applications.

The SEM image after Mn ion adsorption clearly shows a change in the surface morphology of the Mg–Fe LDH compared with that of the prepared material. The layered nanosheet structure observed before adsorption becomes partially covered by irregular deposits and aggregated particles.[51] The surface appears more compact and smoother in some regions, indicating that Mn species have accumulated on the LDH surface and within its pores.

In Fig. 1(h), the image shows that the original layered and sheet morphology of Mg–Fe LDH is partially masked by irregular and agglomerated sheets. The surface appears denser and more compact, indicating that Mn ions have accumulated on the adsorbent surface. In addition, the pore structure reflected the efficiency of the material in methanol oxidation.

Fig. 1(i–k) shows that the material consists of nanosized particles that form agglomerated structures with potential porosity. This morphology provides a high surface area, interparticle voids may enhance mass transfer, and the nanoscale particle size increases the number of active surface sites. These structural characteristics support the material's suitability for manganese adsorption in aqueous systems.

Nitrogen sorption tests were used to determine the mesoporous nature of the LDH (Fig. 1(d and e)). On the basis of the IUPAC classification, the adsorption–desorption isotherms are type IV with an H_3 hysteresis loop, linked to the loops of hysteresis at a relative pressure P/P_0 of the mesoporous characteristics (Fig. 1(d)).

A consistent pore size is further suggested by the extremely low hysteresis between the adsorption and desorption branches (approximately 0.9–1.0 P/P_0). The contact between the material surface and electrolyte is facilitated by the relatively large lateral surface area with the structure of the mesoporous material. Furthermore, the H_3 hysteresis loop implies that the formation of nonuniform slit-shaped pores is caused by the aggregation of plate-like nanoparticles.[52] The surface properties of the prepared sample were estimated by the BET method. The BET surface area, total pore volume and average pore size of the samples are presented in Table 3. The average pore size is

Table 3 Surface properties

Sample name	BET surface area ($m^2\ g^{-1}$)	Total volume of pores ($cm^3\ g^{-1}$)	The mean diameter of pores (nm)
Mg–Fe LDH	260.20	0.136	20.86
Mg–Fe LDH/Mn	6.128	0.136	7.40

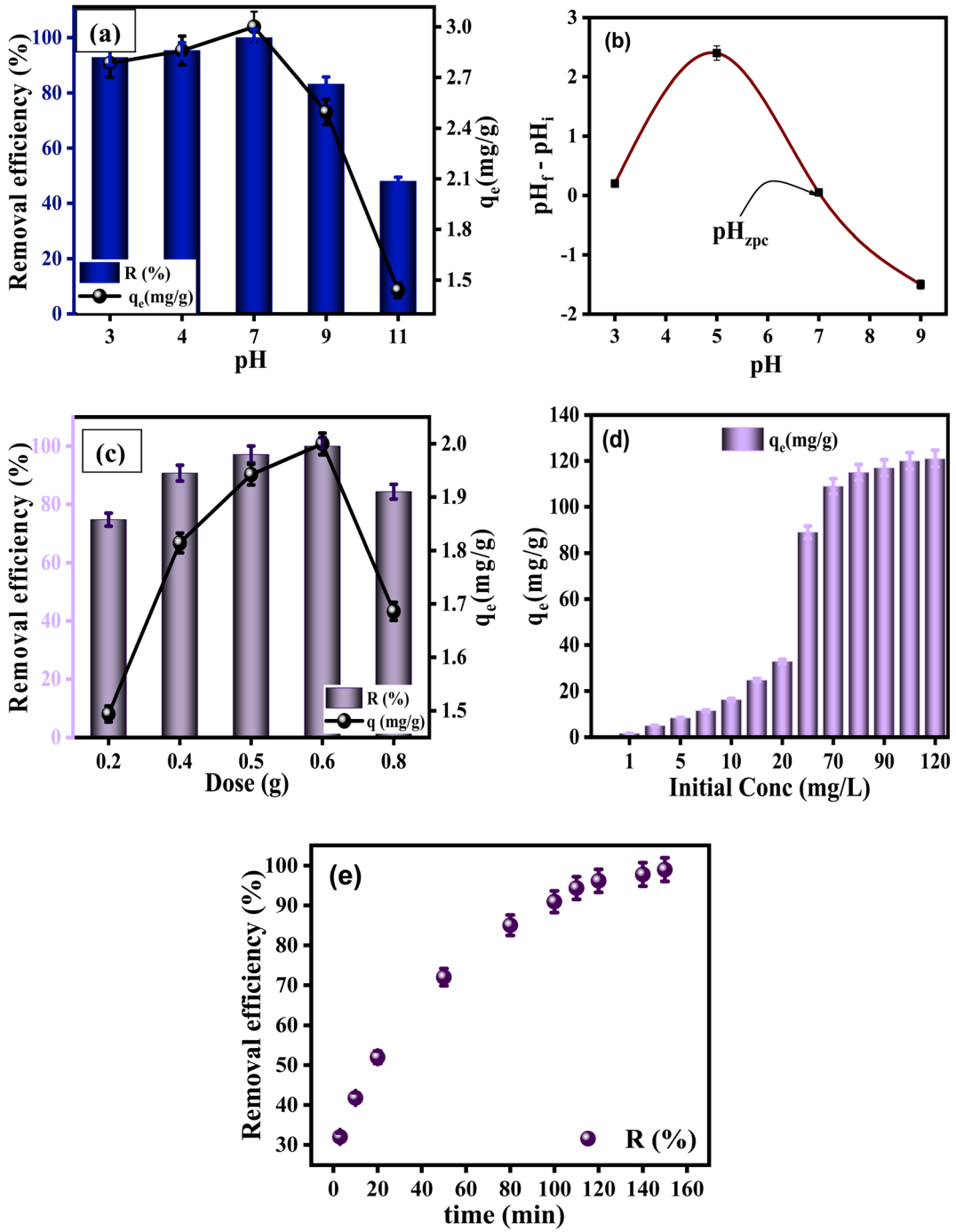

Fig. 2 Removal efficiency % and q_e of Mg–Fe LDH (a) at different pH values, (b) zero charge point of Mg–Fe LDH, (c) at different doses, (d) at different concentrations, and (e) at different times.

<50 nm, and there is extensive pore size spread up to 16 nm (Fig. 1(d and e)).

3.2. Estimation of manganese adsorption

3.2.1. The impact of pH. The pH of the polluted solution was crucial since it regulates the effectiveness of LDH adsorption because of repulsive forces. The effects of the pH (3–11) on heavy metal adsorption are shown in Fig. 2(a), which illustrates the ways in which the solution's pH influences the degree of ionization, the surface charge of the adsorbate, and the adsorbent's selectivity (temperature: 25 ± 1 °C; adsorbent concentration: 0.6 g L^{-1}; and Mn concentration: 10 mg L^{-1}).

While the lowest adsorption capacity was attained at pH values greater than 11, the manganese ions were successfully absorbed at pH 7, demonstrating the best adsorption capacity. Adsorption studies in a pH 7 environment are theoretically optimal. Surface charges of Mg–Fe LDH and the levels of

pollutant dissociation. Hence, the response of the Mg–Fe LDH adsorption system to the pH for the adsorption of manganese was analyzed between pH 3 and 11 (Fig. 2(a)). The presented graphs demonstrate that as the concentration increases, the adsorption percentage increases from 45% to 100% at pH values ranging from 3 to 11, with a maximum clearance of 100% achieved at a pH of 7. Since the surface of the Mg–Fe LDH at neutral pH is significantly negatively charged, which facilitates manganese adsorption on its surface, 7 was chosen as the optimal pH at neutral pH since it demonstrated a notable increase at that pH. As Fig. 2(b) illustrates, 7 was the calculated pH zero-point charge (pH_{PZC}). At pH below 7, the surface of the LDH adsorbent is positively charged, while at pH over 7, it is negatively charged. The surface of LDH has potential surface characteristics for efficient chemical interaction and van der Waals forces (Fig. 2(a)).

The elimination of manganese was low at pH 3, as indicated in Fig. 2(a), which may have been caused by the synthesized LDH breaking down in the acidic media and turbidityifying the solution, the pollutant (Mn) and the LDH; however, both have many negative charges on their surfaces at a higher pH of 11, which causes a vigorous reaction.

3.2.2. Impact of the dosage of adsorbent. Several adsorbent dosages (0.20 g to 0.80 g L^{-1}) were applied to evaluate the effectiveness of the adsorption process. The adsorption rate increases dramatically as the Mg–Fe LDH dose increases to 0.6 g L^{-1} as a result of the presence of more active sites, as shown in Fig. 2(c). After that, any increase in the dose resulted in a decrease in the amount of manganese adsorbed on the Mg–Fe LDH. The particles of the adsorbent are properly dispersed in the solution; this may be connected to areas where the sites for material exchange and adsorption are more accessible.

3.2.3. Impact of the initial concentration of Mn(II). Mn(II) metal ions were adsorbed onto LDH at 0.6 g L^{-1} of adsorbent and stirred at 160 rpm and a pH of 7. The initial Mn(II) concentration (1–100 mg L^{-1}) was investigated. The data in Fig. 2(d) demonstrate that the adsorption capacity of Mg–Fe LDH gradually increases as the concentration of Mn(II) metal ions in the solution steadily increases. Due to the driving force for mass transfer and the abundance of accessible active sites that can adsorb the ions, the high availability of active sites that can adsorb the ions (1–70 mg L^{-1}). In the presence of more metal ions more than 70 mg L^{-1}, the velocity of the adsorption procedure slowed as the profile becomes more uniform, this may be attributed to the adsorbent surface approaches saturation.

3.2.4. Influence of contact time. Several investigations have attempted to determine the impact of time. Initial Mn^{+} concentrations (100 ppm), a pH of 7, and an LDH dose of 0.6 g were used for each experiment. As depicted in Fig. 2(e), the timing of contact changed from 5 to 150 minutes, and with longer contact times, the adsorption increased more quickly, approaching equilibrium. for Mg–Fe LDH in approximately 100 minutes. The adsorption percentage at equilibrium was 93% until 150 minutes, at which time the removal efficiency reached 99%. The intensity absorption tends to decrease, even if the absorption does not cause any movement in the wavelength. This is caused by the first stage of rapid adsorption and the decrease in the number of active points on the adsorbent surface.

3.3. Adsorption isotherm

An indication of concentration is the adsorption isotherm, which represents a certain amount of adsorbate per unit of mass of the catalyst. Additionally, it shows and explains how molecules are dispersed at adsorption equilibrium between the liquid and solid phases.[53] Langmuir,[54] Freundlich,[55] Langmuir–Freundlich,[56] and Baudu. Adsorption isotherms were expressed using models.,[57] as shown by eqn (3)–(5), respectively. The Langmuir model was applied for homogenous surface systems, whereas for heterogeneous surface systems, the Freundlich model is used to ensure that as the concentration of adsorbate in the solution increases, the adsorbate concentration on the adsorbent increases.[58]

The Langmuir–Freundlich isotherm model provides information about the movement of adsorption energy on heterogeneous surfaces.[59]

The Langmuir coefficients, K_L and q_{max}, are not constant across a large range, as demonstrated by the tangent measurements at various equilibrium concentrations. The Bauder isotherm model reduces to the Freundlich model for coverage of the lower surface. The isotherm variables were determined using nonlinear regression analysis. All of the parameters related to these isotherm models are provided in Table 4.

From Fig. 3(a) and Table 4, the correlation coefficient (R^2) and q_{max} (mg g^{-1}) were obtained from the nonlinear plot of C_e *vs.* q_e. The fitting data demonstrated that the Langmuir–Freundlich model is capable of providing a sufficient explanation for LDH isotherm operations. R^2 was 0.998, and q_{max} was 198.99 mg g^{-1} for LDH. This could be explained by the strong chemical interactions that occur between metal ions and heavy metals, as well as the large surface area and pore volume of the adsorbent.

The Langmuir–Freundlich model is especially suitable for heterogeneous systems because it combines the surface heterogeneity concept of the Freundlich equation with the monolayer adsorption assumption of the Langmuir model. In comparison to the Freundlich ($R^2 = 0.992$) and Langmuir ($R^2 = 0.981$) isotherms, the Langmuir–Freundlich isotherm had the best correlation coefficient ($R^2 = 0.998$) among the investigated models. This figure represents the theoretical monolayer adsorption capacity of Mn(II) on Mg–Fe LDH. Compared with the classic Langmuir model, the Langmuir–Freundlich model produced a greater q_{max} (198.99 mg g^{-1}), suggesting that the adsorption process does not occur on an energetically homogenous surface. Instead, it shows the participation of various types of active sites, including edge sites, external hydroxyl groups, and possible interlayer interactions that are typical of layered double hydroxide.

0.014 L mg^{-1} (K) is the affinity constant. The K_{LF} parameter indicates how strongly Mn(II) ions bind with the adsorption sites. Its magnitude indicates favorable adsorption and suggests that the absorption process is significantly influenced by surface complexation mechanisms and electrostatic attraction between Mn^{2+} and surface functional groups (M–OH). The

Table 4 Factors of the isotherm models

Isotherm models	Expression	Adjustable model parameters[a]	Values	R^2
Two-parameters isotherm				
Langmuir	$q_e = \frac{q_{max} K_L C_e}{1 + K_L C_e}$ (3)	q_{max}	90	0.981
		K_L	0.00168	
Freundlich	$q_e = K_f C_e^{1/n_f}$ (4)	K_f	2.89	0.992
		$1/n_f$	0.82	
Three-parameters isotherm				
Langmuir–Freundlich	$q_e = \frac{q_{max}(K_{LF} C_e)^{\beta_{LF}}}{1 + (K_{LF} C_e)^{\beta_{LF}}}$ (5)	q_{max}	198.99	0.998
		K_{LF}	0.014	
		β_{LF}	1.235	

[a] q_e refers to amount of adsorbate in the adsorbent at equilibrium (mg g^{-1}); C_e is the equilibrium concentration (mg L^{-1}); q_{max} is the maximum adsorption capacity (mg g^{-1}); K_L is Langmuir adsorption constant (L mg^{-1}); K_f is Freundlich adsorption capacity (mg g^{-1}); 1/nf is Freundlich adsorption intensity; K_{LF} is Langmuir-Freundlich equilibrium constant for heterogeneous solid; β_{LF} is the Langmuir-Freundlich heterogeneous parameter.

heterogeneity parameter is $\beta_{LF} = 1.235$. The deviation of the β value from unity confirms the heterogeneity of the surface energy. Structural components such as edge hydroxyl groups, different Fe/Mg coordination environments, and positively charged brucite-like layers are responsible for this variance in Mg–Fe LDH. Adsorption may involve increased binding at some high-energy sites at low Mn(II) concentrations, followed by the occupation of lower-energy sites as the concentration increases if the β value is greater than 1.

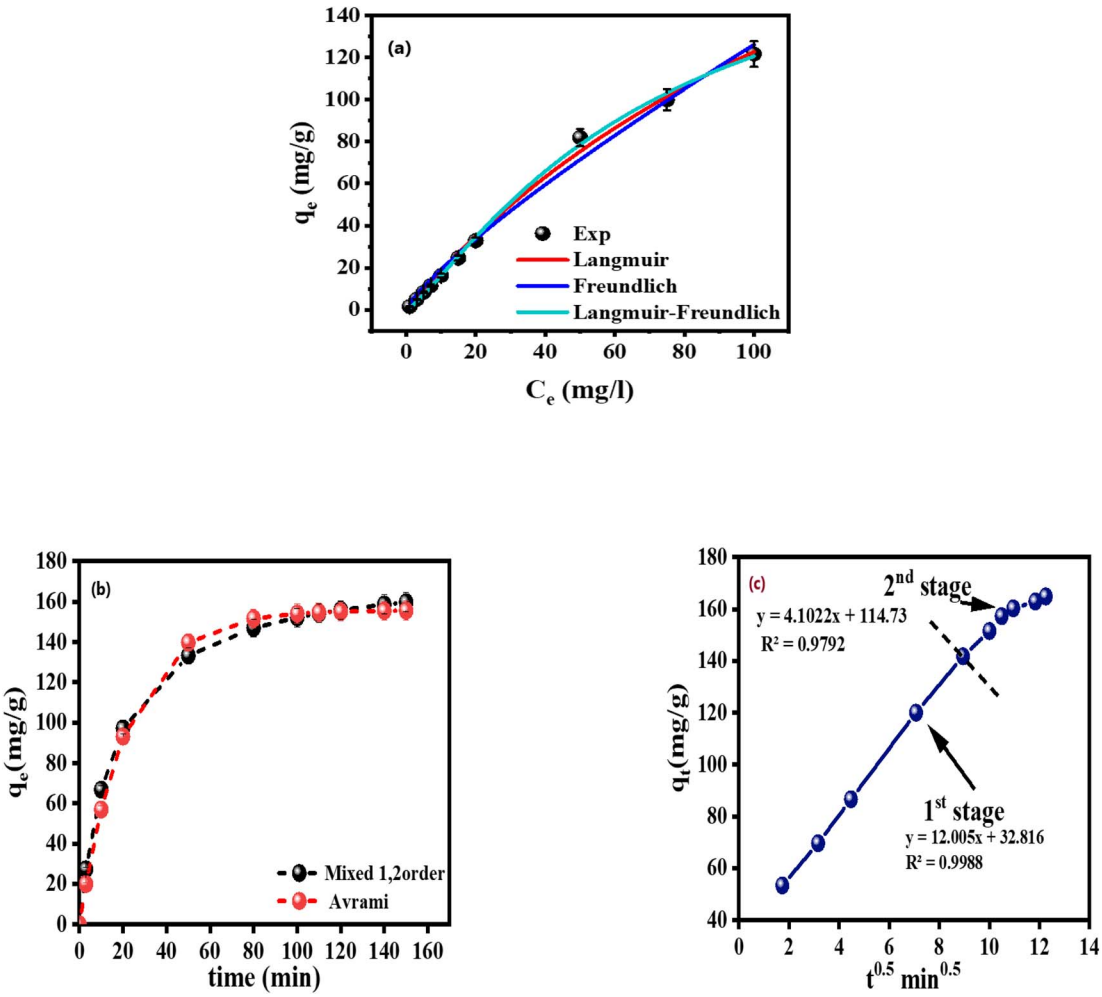

Fig. 3 Applying (a) adsorption isotherm models and (b and c) kinetic isotherm models.

Therefore, the superiority of the Langmuir–Freundlich model suggests that a heterogeneous monolayer adsorption process including nonequivalent binding sites controls Mn(II) adsorption onto Mg–Fe LDH as opposed to perfect Langmuir-type behavior.

3.4. Adsorption kinetics models

Kinetics studies are crucial in the construction of adsorbents because they offer essential information on the processes and absorption rates of contaminants. Our study clarified how pseudo-first-order, pseudo-second-order, mixed 1,2-order Avrami, and intraparticle diffusion occur. Additionally, it might be applied to describe the kinetics of contaminant elimination.

While f_2 is the dimensionless coefficient and k is the constant of the adsorption rate (mg g^{-1} min^{-1}) of the mixed 1,2-order model, k is the rate constant (min^{-1}) and is a component of the Avrami model; q_t and q_e are similar to those of the pseudo-first-order model, pseudo-second-order, mixed 1,2-order, intraparticle diffusion and Avrami. Comparisons of the fit qualities of the three kinetic models. Every nonlinear fit q_t *vs.* t was evaluated for beauty. A nonlinear plot of t *vs.* q_t was computed for each models, and (Fig. 3(b and c)) displays the results. The model coefficients are shown in Table 5. An analysis of the regression coefficients for each model revealed that the estimated and experimental values of $q_{(max)}$ and kinetic constants provided the best results for the behavior of Mn adsorption on Mg–Fe LDH fitted with intraparticle diffusion and mixed 1,2-order models, according to the significant correlation coefficient (0.965 and 0.964, respectively) given by the intraparticle diffusion and mixed 1,2-order models.

Several models, including pseudo-first-order, pseudo-second-order, mixed 1,2-order, Avrami, and intraparticle diffusion, were used to examine the adsorption kinetics of the LDH material. The data were not well represented by the pseudo first- and pseudo-second-order models (R^2 = 0.478 and 0.47, respectively), suggesting that adsorption cannot be explained by a single process such as chemisorption or simple physisorption. On the other hand, the mixed 1,2-order and intraparticle diffusion models showed excellent fits (R^2 = 0.964 and 0.965, respectively), indicating that a mixture of surface contacts and diffusion within the mesopores controls the process. An intraparticle diffusion study verified that pore diffusion strongly affects the rate, whereas the high F_2 value (0.97) in the mixed-order model shows that physisorption is predominant, with a small contribution from chemisorption.

A complicated, multistep adsorption process involving heterogeneous sites is further supported by the Avrami model (R^2 = 0.934). In general, adsorption occurs quickly at the surface at first, after which diffusion into the pores occurs more slowly and becomes the rate-limiting process. These findings demonstrate that adsorption on LDH is regulated by mixed 1,2-order and intraparticle diffusion and that adsorption occurs *via* the interlayer space and on the surface, which is associated with the mesoporous structure and surface area of Mg–Fe LDH.

3.5. Effect of temperature

The data in Fig. 4 further demonstrate how increasing the temperature accelerates the process by which Mn(II) ions bind to the adsorbent surface. A thermodynamic approach can be used to investigate the adsorption equilibrium. The most common assumption in the context of thermodynamics is that the adsorbed layer can be distinguished from the bulk phase. Because of this, there are a few distinct ways to approach the application of thermodynamic concepts to adsorption equilibrium. The adsorbed surface layer of the adsorbate can be regarded as a single phase with bulk solution-like characteristics. However, it is believed that the adsorbents are thermodynamically inert.

At equilibrium, the rate at which the adsorbate is adsorbed onto the adsorbent surface is equal to the rate at which it is

Table 5 Parameters for the LDH adsorption kinetic models

Kinetic models	Equation	Parameters	LDH
Pseudo-first-order	$q_t = q_e(1 - e^{-k_1 t})$ (6)	K_1	41.75
		Q_e	126.87
		R^2	0.478
Pseudo-second-order	$q_t = \frac{q_e^2 k_2 t}{1 + q_e k_2 t}$ (7)	K_2	1.03×10^6
		Q_e	126.87
		R^2	0.47
Mixed 1,2 order	$q_t = q_e \frac{(1 - \exp(-kt))}{1 - f_2 \exp(-kt)}$ (8)	K	0.0014
		Q_e	175.44
		F_2	0.97
		R^2	0.964
Avrami	$q_t = q_e[-1 - \exp(-k_{av}t)_{av}^{n}]$ (9)	Q_e	155.76
		K_{av}	0.214
		n_{av}	0.215
		R^2	0.934
Intraparticle diffusion	$q_t = K_{ip}\sqrt{t} + C_{ip}$ (10)	K_{ip}	12.54
		C_{ip}	23.08
		R^2	0.965

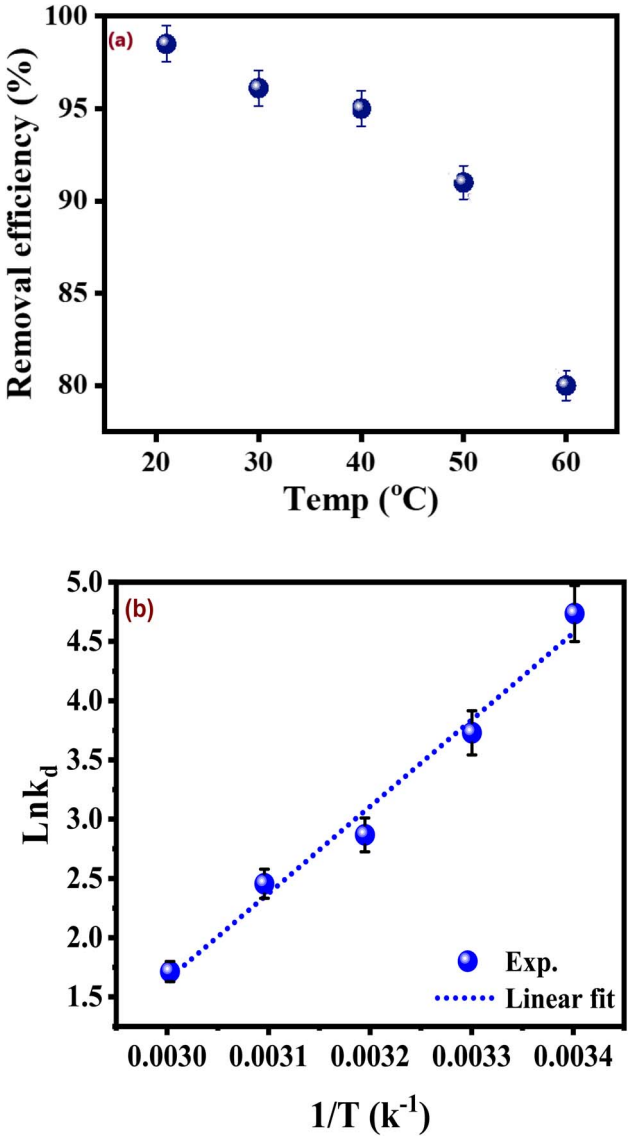

Fig. 4 Effect of temperature on the Mn removal efficiency percentage (a), ln K_d *versus* inverted temperature 1/T (K^{-1}) (b).

desorbed from the adsorbent surface. The amount of adsorbate in the aqueous solution and on the adsorbent surface becomes nearly constant.[60] The optimal factors (0.6 g dose of adsorbent per 50 mL, pH = 7, 100 ppm concentration of Mn, until balance) should be used to calculate the thermodynamic parameters at different temperatures (20, 30, 40, 50, and 60 °C). The mixed order rate constant, which is represented in the Arrhenius form, can be used to calculate the energy of activation for manganese adsorption.[61]

$$\ln k_2 = \ln\ k_o - E/RT \tag{11}$$

where T is the temperature (K), R is the gas constant (8.314 J mol^{-1} K^{-1}), E is the activation energy (J mol^{-1}), and k_o is the equation's constant (g mg^{-1})min^{-1}. According to eqn (11), the rate constants change with temperature, as shown in Fig. 4(a). The slope of the fitted equation indicates that the activation energy for manganese is 21.01 kJ mol−1. The equilibrium constant (K), standard free energy change ($\Delta G°$), and free energy change (ΔG) at constant temperature (T) are correlated by the classic van't Hoff reaction isotherm equation as follows:

$$\Delta G = \Delta G^{\circ} + RT \ln K \tag{12}$$

Since the free energy change (ΔG) is zero at equilibrium, eqn (13) decreases as follows:

$$\Delta G^{\circ} = -RT \ln K \tag{13}$$

The spontaneous nature of adsorption is reflected by a negative value of ΔG. Using the van't Hoff method, other thermodynamic parameters, including the change in enthalpy (ΔH) and the change in entropy (ΔS), were assessed (Fig. 4(b)).

$$\mathrm{Ln}\ K_d = \Delta S/R - \Delta H/RT \tag{14}$$

The negative Gibbs free energy values (−4.58 to −10.50 kJ mol^{-1}) across the studied temperature range (298–333 K) confirm that the adsorption process is spontaneous. The magnitude of $\Delta G°$ falls within the typical range reported for adsorption systems, indicating a thermodynamically feasible process rather than an excessively strong interaction. When manganese adsorbs on the adsorbent, the solution interface becomes more random and absorbs heat from the environment, as indicated by negative changes in entropy measurements.[62] The thermodynamic conditions for the process of Mn adsorption onto the prepared materials are listed in Table 6.

The negative enthalpy change ($\Delta H° = -60.83$ kJ mol^{-1}) indicates that the adsorption of Mn onto LDH is exothermic. This suggests that Mn binding likely involves strong surface interactions such as surface complexation and ion exchange with hydroxyl groups within the LDH layers. The relatively high magnitude of $\Delta H°$ further supports the contribution of chemisorption mechanisms. The negative entropy change ($\Delta S° = -168.89$ J mol^{-1} K^{-1}) indicates a decrease in randomness at the solid–solution interface during adsorption. This can be attributed to the immobilization of Mn ions onto well-defined active sites of the LDH structure and possible structural ordering of water molecules around the adsorbed species. Furthermore, this is consistent with the exothermic nature of the process because greater temperatures decrease the degree of adsorption favorability, as reflected by the steady increase in the $\Delta G°$ values (which become less negative) with increasing temperature. This

Table 6 Thermodynamic conditions for the process of Mn adsorption onto prepared materials

T (K)	$\Delta G°$ (kJ mol^{-1})	$\Delta H°$ (kJ mol^{-1})	$\Delta S°$ (J mol^{-1} K^{-1})
298	−10.50	−60.83	−168.890
303	−9.65	−60.83	−168.890
313	−7.95	−60.83	−168.890
323	−6.27	−60.83	−168.890
333	−4.58	−60.83	−168.890

behavior provides more evidence that Mn uptake efficiency is improved at lower temperatures.

Overall, the thermodynamic parameters confirm that Mn adsorption onto LDH is an exothermic, spontaneous process controlled by strong surface contact and a reduction in interfacial disorder.

3.6. Mechanism of manganese adsorption on Mg–Fe LDH

The manganese adsorption process on Mg–Fe layered double hydroxide (LDH) is governed by a combination of surface complexation, chemical interaction and interlayer space. The positively charged brucite-like layers of Mg–Fe LDH, resulting from the isomorphic substitution of Mg^{2+} by Fe^{3+}, are charge balanced by interlayer anions and water molecules.

At circumneutral pH (pH = 7), Mn^{2+} ions interact strongly with surface hydroxyl groups (≡M–OH, where M = Mg or Fe), forming inner-sphere complexes through ligand exchange reactions. This interaction is supported by shifts in FTIR bands associated with hydroxyl stretching and metal–oxygen vibrations. Simultaneously, partial replacement of interlayer anions by Mn-containing species may occur.

The adsorption kinetics follow the mixed 1,2-order and intraparticle diffusion models, indicating that chemisorption is the rate-limiting step. Thermodynamic analysis confirms that the process is spontaneous and exothermic, suggesting strong metal–surface interactions rather than weak physical adsorption.

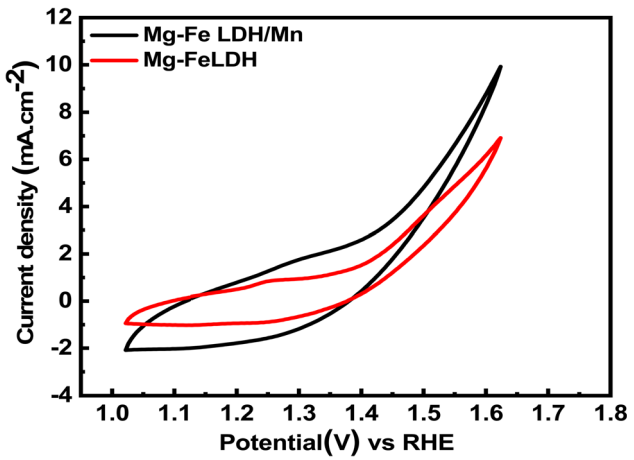

Fig. 5 Electrocatalytic activity of Mg–Fe LDH and Mg–Fe LDH/Mn toward methanol (1.0 M) oxidation.

4 Electrochemical studies

All the electrochemical experiments were carried out utilizing a potentiostat/galvanostat (AUTOLAB-PGSTAT 302 N, Metrohm) for the Mg–Fe LDH and Mg–Fe LDH/Mn nanocomposites. With a voltage window of 0 to 0.1 V in 0.5 M NaOH, cyclic voltammetry (CV) measurements were carried out at different scan rates. Electrolyte solution at varying methanol concentrations. The 0.6 V step potential is where the chronoamperometric test is applicable.

4.1. Catalytic performance of methanol electro-oxidation

Fig. 5 demonstrated the electrocatalytic activity of pure LDH and Mn-containing (10 wt%) LDH toward methanol oxidation (MOR). The measurements were performed at 25 °C with a scan rate of 100 mV s^{-1} in an electrolyte that included 1.0 M methanol dissolved in 0.5 M NaOH.

Both catalysts clearly show electrocatalytic activity toward methanol oxidation in alkaline environments, according to the cyclic voltammograms. Interestingly, the electrocatalytic response of the Mn-modified Mg–Fe LDH catalyst is much greater than that of the pure LDH. The increased current density and the shift of the methanol oxidation peak toward more advantageous potentials (compared with RHE) are

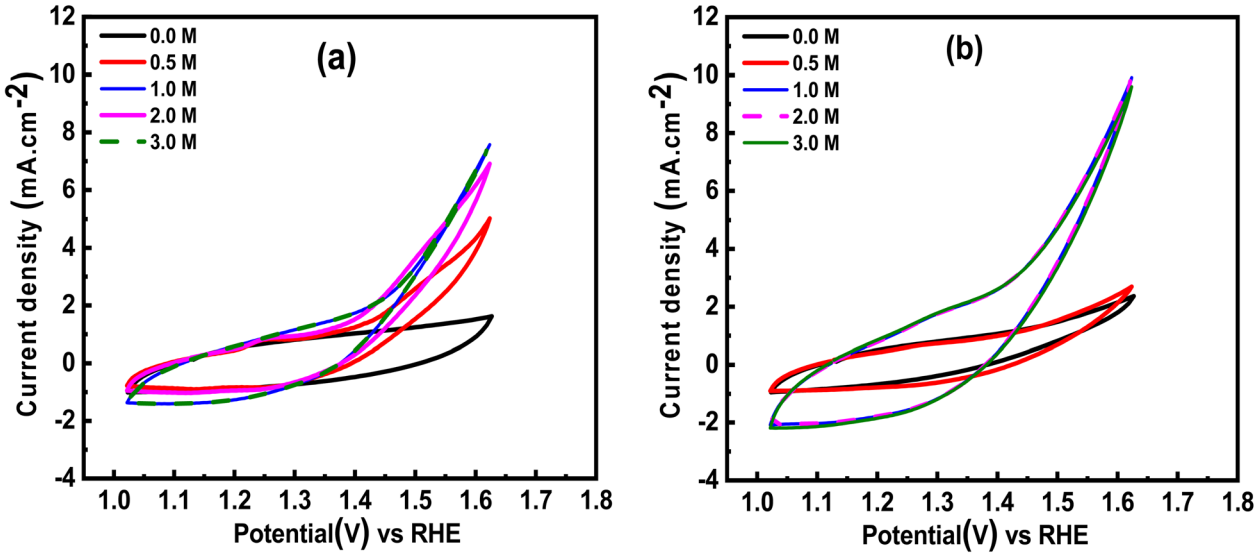

Fig. 6 Influence of the methanol concentration (a) Mg–Fe LDH, (b) Mg–Fe LDH/Mn, at 50 mV s^{-1}.

indicative of this improvement. The altered surface shape and the presence of Mn species, which probably accelerate charge transfer and offer more active sites for methanol adsorption and oxidation, are responsible for the increased catalytic activity. These results proved that the presence of Mn in the structure of LDH plays an important role in improving the electrocatalytic efficiency toward methanol oxidation.

Therefore, various methanol concentrations ranging from 0.5 to 3.0 M in the presence of 0.5 M NaOH were examined at a scan rate of 100 mV s^{-1}. As the methanol concentration increased, the current density of methanol significantly increased (Fig. 6). Adsorption of methanol on the catalyst surface is the initial stage of the oxidation process, which employs a three-electron transfer mechanism. The current density may increase with increasing methanol concentration because of the large concentration of electroactive sites on the catalyst surface. The LDH support also decreases catalyst aggregation and improves the conductivity and surface area. A four-electron process that converts methanol into several intermediates, such as CH_2OH, CHOH, COH, and CO, may be used in the next step. Hydroxide anions adsorbed on the catalyst surface can help oxidize and purify CO, even when CO poisons the active sites. The suggested mechanism is given below under ideal conditions (1 bar, 298 K).[63,64]

$$\text{Anode: } CH_3OH + 6OH^- \rightarrow CO_2 + 6e^- + 5H_2O \ (E_a = -0.81\ \text{V}) \quad (15)$$

$$\text{Cathode: } 3/2O_2 + 6e^- + 3H_2O \rightarrow 6OH^- \ (E_c = 0.40\ \text{V}) \quad (16)$$

$$\text{Overall reaction: } CH_3OH + 3/2O_2 \rightarrow CO_2 + 2H_2O \ (E_{cell} = 1.21\ \text{V}) \quad (17)$$

When the scan rate varies, the migration of OH^- into the mesopore cavities controls the electrochemical process, which ultimately results in an increase in redox reactions during the activation stage.[65]

4.2. Effect of methanol concentration

The electrochemical activity of Mg–Fe LDH (Fig. 6(a)) and Mg–Fe LDH/Mn (Fig. 6(b)) was examined at a scan rate of 100 mV s^{-1} and at various concentrations of 0.0 M, 0.5 M, 1 M, 2 M, and 3 M methanol. When the MeOH concentration increased from 0.5 M to 3 M, the current density increased for Mg–Fe LDH and Mg–Fe LDH/Mn, demonstrating their significant electron generation and electroactivity for methanol oxidation, with current densities of 7.86 mA cm^{-2} and 10.5 mA cm^{-1-2}, respectively. Stronger methanol oxidation peaks are observed for both LDH and LDH/Mn at 3 M, suggesting that the methanol oxidation process has run out of active sites. This diffusion phenomenon causes a rise in the reaction rate in response to an increase in the methanol concentration, which in turn promotes methanol oxidation. At 3 M methanol, their oxidation peak was higher.

4.3. Effect of scan rate

As shown in Fig. 7, the effect of mass transfer on the electrochemical reaction rate can be estimated using the CVs of Mg–Fe LDH and Mg–Fe LDH/Mn in 1.0 M NaOH + 1 M methanol for different scans (5, 10, 20, 30, 40, 50, 80 and 100 mV s^{-1}). It was evident that the scan rate affected the generated current density, which confirms that the mass transfer capabilities of the catalyst's nanosheet structure increased. Because of the stronger electrochemical characteristics of Mg and Fe with the Mn ions, which give the LDH more active sites, a greater current density was demonstrated for Mg–Fe LDH/Mn.

The observed relationship between the current density and scan rate indicates that the electrochemical process is predominantly surface controlled rather than diffusion limited. This behavior suggests that methanol oxidation occurs through the adsorption of methanol molecules onto the active catalytic

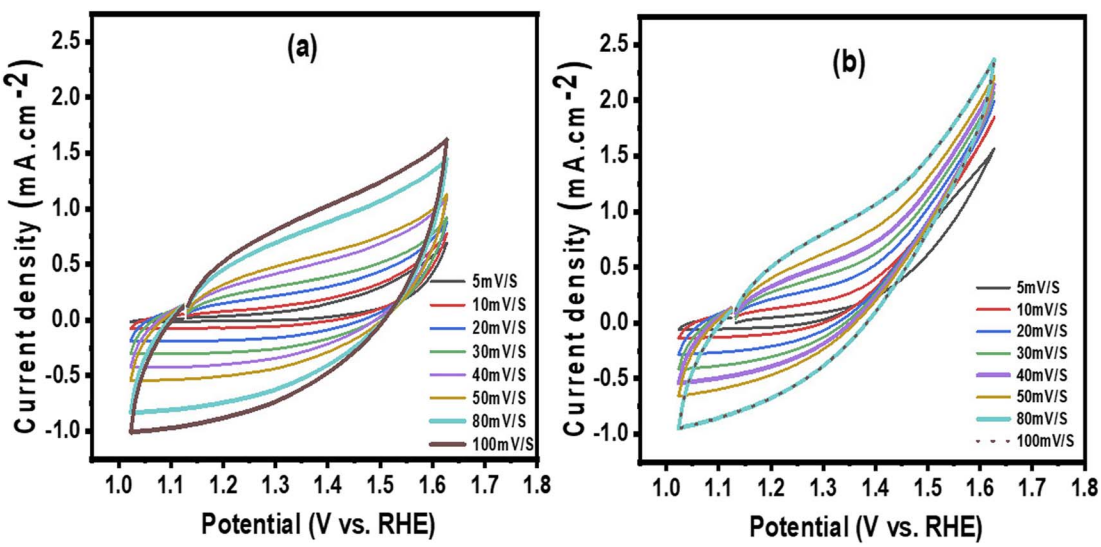

Fig. 7 Effect of the different scan rates on (a) Mg–Fe LDH and (b) Mg–Fe LDH/Mn in 1.0 M NaOH + 1.0 M MeOH.

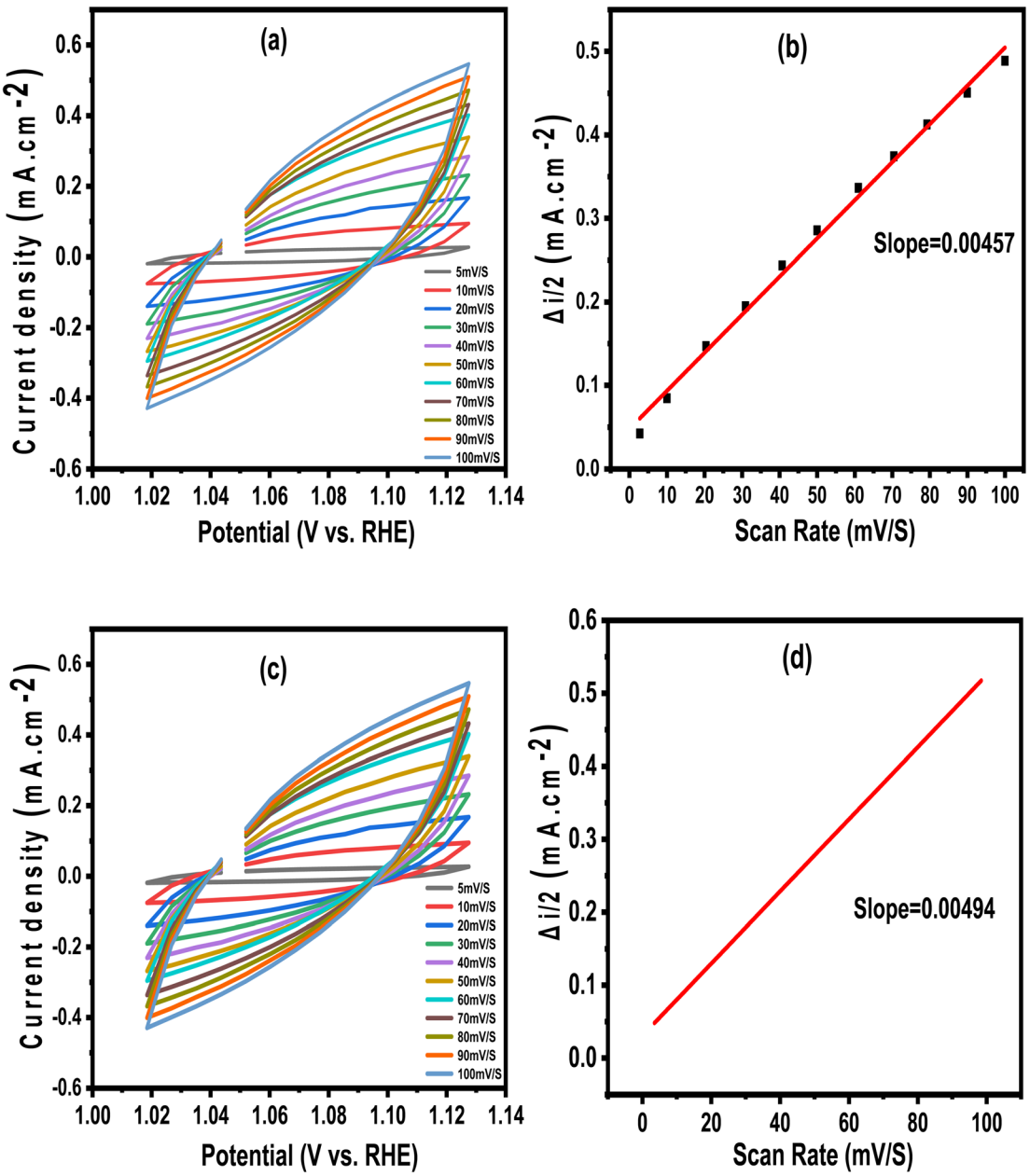

Fig. 8 Cyclic voltammograms recorded at various scan rates in the nonfaradaic potential region for (a) LDH & (c) LDH/Mn and (b) & (d) a linear plot of the capacitive current density (Δi) *versus* the scan rate used to determine the double-layer capacitance (C_{dl}) for LDH & LDH/Mn.

sites, followed by successive dehydrogenation and oxidation steps. Both methanol and hydroxyl species are adsorbed on the catalyst surface prior to the surface reaction. In addition, the presence of surface hydroxyl groups facilitates the oxidative removal of adsorbed intermediate species (*e.g.*, CO_ads), which is typically described by a bifunctional mechanism in alkaline media.

As a result, the scan-rate-dependent analysis revealed that the rate-determining step is connected to the surface reaction between adsorbed intermediates and surface hydroxyl species and offers further experimental evidence for the suggested reaction pathway.

4.4. Evolution of the electrochemically active surface area (ECSA) *via* double-layer capacitance (C_{dl})

The electrochemically active surface area (ECSA) was estimated from the double-layer capacitance (C_{dl}). Cyclic voltammetry was performed in a nonfaradaic potential window at different scan rates (5–100 mV s^{-1}). The difference in the capacitive current density ($\Delta i = i_a - i_c$)/2 was plotted against the scan rate, and the slope of the linear fit corresponds to C_{dl}.

ECSA was calculated using the following equation:

$$\mathrm{ECSA} = C_{dl}/C_s, \quad (18)$$

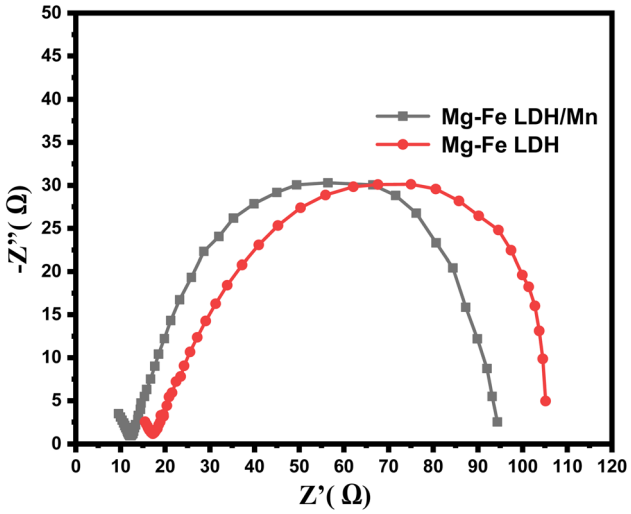

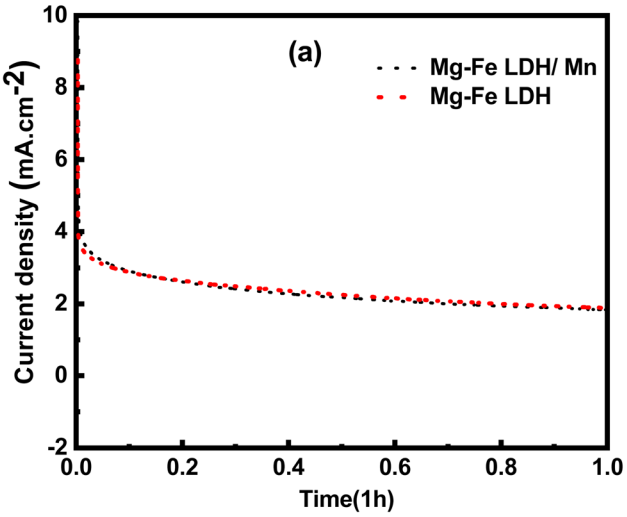

Fig. 9 Electrochemical impedance spectroscopy (EIS) for Mg–Fe LDH and Mg–Fe LDH/Mn electrodes.

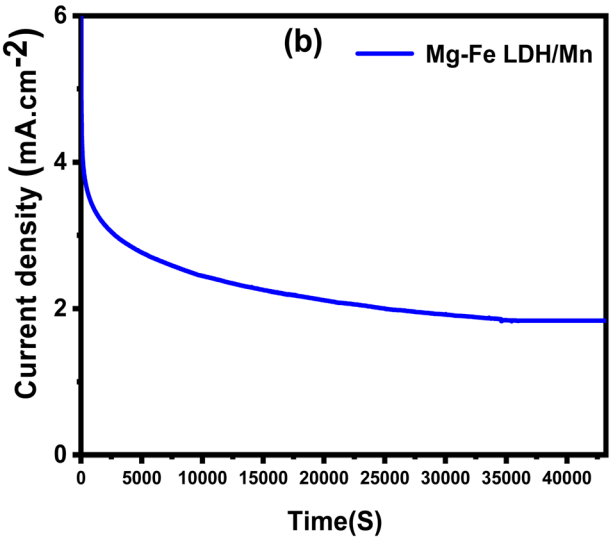

Fig. 10 Stability of (a) Mg–Fe LDH and Mg–Fe LDH/Mn electrodes for 1 h and (b) Mg–Fe LDH/Mn electrode for 12 h.

The double-layer capacitance (C_{dl}) obtained from cyclic voltammetry measurements in the nonfaradaic region at various scan rates (5–100 mV s^{-1}) was used to calculate the electrochemically active surface area (ECSA) of the catalyst. The prevailing capacitive behavior is confirmed by the capacitive current density (Δi), which is linearly related to the scan rate. As shown in Fig. 8(b) and (d), the slopes obtained from the linear fitting of the (Δi) *versus* scan rate plot were 0.00457 and 0.0049 for LDH and LDH/Mn, respectively. The calculated double-layer capacitance values are 0.0049 and 0.00457 mF cm^{-2}, corresponding to ECSA values of 0.114 cm^2 and 0.1225, respectively. Higher C_{dl} and ECSA values indicate a greater density of electrochemically active sites.

It corresponds to a C_{dl} value of 0.00457 mF cm^{-2} and 0.0049 mF cm^{-2}. A significant number of electrochemically accessible active sites may be present, as shown by the comparatively high C_{dl} value, which enhances the electrocatalytic efficacy.

4.5. Electrochemical impedance spectroscopy (EIS)

The charge transfer kinetics and interfacial characteristics of the produced materials were examined using electrochemical impedance spectroscopy (EIS). According to Fig. 9, the charge transfer resistance (R_{ct}) and diffusion-controlled process (Warburg impedance) are represented by a depressed semicircle in the high- to medium-frequency region and a straight line in the low-frequency region, respectively. The semicircle diameter of the Mg–Fe LDH/Mn composite is noticeably smaller than that of the pristine Mg–Fe LDH, indicating a reduced charge transfer resistance and enhanced electrical conductivity.

This behavior indicates that the addition of Mn efficiently accelerates the electrochemical reaction kinetics by facilitating electron transport at the electrode–electrolyte interface. The additive impact of Mn, which enhances the electronic pathways and increases the accessibility of active sites, is responsible for the improved electrochemical performance. These results are consistent with the structural and morphological features seen in the XRD and SEM analyses, which reveal enhanced crystallinity and a more homogeneous layered morphology that promotes electron transfer and ion diffusion. Thus, it is evident from the EIS data that Mn modification significantly improved the overall electrochemical activity and interfacial charge transfer process of the Mg–Fe LDH-based material.

4.6. Chronoamperometric test

The stability of the electrocatalysts was investigated in 2 M methanol and 0.5 M NaOH for Mg–Fe LDH and Mg–Fe LDH/Mn (Fig. 10(a)). Chronoamperometry was used to measure the stability of the nanomaterials at a potential step of 0.6 V for an hour. The current density initially decreased rapidly because of the contribution of the double layer, but it gradually decreased as carbonaceous intermediate CO adsorbed.[66] Compared with

Mg–Fe LDH and Mg–Fe LDH/Mn, the long-term stability that is offered is that of Mg–Fe LDH/Mn.

The stability of the Mg–Fe LDH/Mn catalyst was evaluated using chronoamprometric measurements over a 12-hour period (Fig. 10(b)). This experiment demonstrated the catalyst's efficiency long-term durability.

5 Conclusions

In this study, Mg–Fe Layered Double Hydroxides (LDH) were synthesized and evaluated as efficient adsorbents for Mn(II) ions. The maximum adsorption capacity of the Mg–Fe LDH q_{max} was 198.99 mg g^{-1}. The pH of the medium significantly influenced the removal efficiency, with point-of-zero-charge (PZC) measurements indicating an optimal pH of 7. The optimal adsorbent dosage was determined to be 0.6 g L^{-1}, achieving complete (100%) Mn(II) removal under stirring at 640 rpm for 120 minutes at room temperature. The adsorption process was exothermic nature. Furthermore, the synthesized Mg–Fe LDH and Mg–Fe LDH/Mn materials exhibited strong electrocatalytic activity for methanol oxidation, highlighting their multifunctional potential in both adsorption and electrocatalysis applications.

Consent to publish

The authors declare that they consent to publish this paper.

Consent to participate

The authors declare that they consent to participate in the work.

Author contributions

Writing – original draft, data curation, formal analysis, and investigation: Norhan Badawy and Amna A. Kotp; formal analysis: Ahmed Farghali; conceptualization, supervision, visualization: Amal Zaher, Rehab Mahmoud; writing – review & editing: Rehab Mahmoud, and Amal Zaher.

Conflicts of interest

The authors have no conflicts of interest to declare.

Data availability

The datasets used and/or analyzed during the current study available from the corresponding author on reasonable request.

References

1 M. Shamrukh and A. Abdel-Wahab, Water Pollution and Riverbank Filtration for Water Supply along River Nile, Egypt, in *Riverbank Filtration for Water Security in Desert Countries*, Springer, 2011, pp. 5–28.

2 C. Ray and M. Shamrukh, *Riverbank Filtration for Water Security in Desert Countries*, Springer Science & Business Media, 2010.

3 S. M. Ezzat, H. M. Mahdy, E. H. Abd El Shakour, and M. A. El-Bahnasawy. *Water Quality Assessment of River Nile at Rosetta Branch: Impact of Drains Discharge*, 2012.

4 W. Blanford, T. Boving, Z. Al-Ghazawi, M. Shawaqfah, J. Al-Rashdan, I. Saadoun, J. Schijven and Q. Ababneh, River Bank Filtration for Protection of Jordanian Surface and Groundwater, in *World Environmental and Water Resources Congress 2010: Challenges of Change*, 2010, pp. 776–781.

5 N. Marsidi, H. A. Hasan and S. R. S. Abdullah, A Review of Biological Aerated Filters for Iron and Manganese Ions Removal in Water Treatment, *J. Water Process Eng.*, 2018, **23**, 1–12.

6 M. F. Bouchard, C. Surette, P. Cormier and D. Foucher, Low Level Exposure to Manganese from Drinking Water and Cognition in School-Age Children, *Neurotoxicology*, 2018, **64**, 110–117.

7 J. B. Marcus, Chapter 7-Vitamin and Mineral Basics: The ABCs of Healthy Foods and Beverages, Including Phytonutrients and Functional Foods: Healthy Vitamin and Mineral Choices, Roles and Applications in Nutrition, Food Science and the Culinary Arts, In *Culinary Nutrition*, 2013, pp. 279–331.

8 A. K. Rose, L. Fabbro and S. Kinnear, Hydrogeochemistry in a Relatively Unmodified Subtropical Catchment: Insights Regarding the Health and Aesthetic Risks of Manganese, *J. Hydrol.: Reg. Stud.*, 2017, **13**, 152–167.

9 E. L. Cochrane, S. Lu, S. W. Gibb and I. Villaescusa, A Comparison of Low-Cost Biosorbents and Commercial Sorbents for the Removal of Copper from Aqueous Media, *J. Hazard. Mater.*, 2006, **137**(1), 198–206.

10 R. Davarnejad and P. Panahi, Cu (II) Removal from Aqueous Wastewaters by Adsorption on the Modified Henna with Fe3O4 Nanoparticles Using Response Surface Methodology, *Sep. Purif. Technol.*, 2016, **158**, 286–292.

11 L. Wang, J. Zhang, J. Liu, H. He, M. Yang, J. Yu, Z. Ma and F. Jiang, Removal of Bromate Ion Using Powdered Activated Carbon, *J. Environ. Sci.*, 2010, **22**(12), 1846–1853.

12 Z. Arwidsson, K. Elgh-Dalgren, T. von Kronhelm, R. Sjöberg, B. Allard and P. van Hees, Remediation of Heavy Metal Contaminated Soil Washing Residues with Amino Polycarboxylic Acids, *J. Hazard. Mater.*, 2010, **173**(1–3), 697–704.

13 A. Violante, M. Pucci, V. Cozzolino, J. Zhu and M. Pigna, Sorption/Desorption of Arsenate on/from Mg–Al Layered Double Hydroxides: Influence of Phosphate, *J. Colloid Interface Sci.*, 2009, **333**(1), 63–70.

14 A. Mahmoud, F. I. A. El-Ela, R. Mahmoud, A. Z. Shehata, H. Abd El-Raheem, E. Salama, A. A. Allam, H. E. Alfassam and A. Zaher, Eco-Friendly Moxifloxacin Removal Using Date Seed Waste and Ni-Fe LDH: Adsorption Efficiency and Antimicrobial Potential, *Ecotoxicol. Environ. Saf.*, 2025, **297**, 118256.

15 S. A. Aita, R. Mahmoud, S. H. M. Hafez and A. Zaher, Investigating Adsorption of Aqueous Heavy Metals through

Isotherms and Kinetics with Zn-Co-Fe/LDH for Remarkable Removal Efficiency, *Appl. Water Sci.*, 2025, **15**(4), 75.

16 R. Mahmoud, N. M. Kotb, Y. GadelHak, F. I. A. El-Ela, A. Z. Shehata, S. I. Othman, A. A. Allam, H. A. Rudayni and A. Zaher, Investigation of Ternary Zn–Co–Fe Layered Double Hydroxide as a Multifunctional 2D Layered Adsorbent for Moxifloxacin and Antifungal Disinfection, *Sci. Rep.*, 2024, **14**(1), 806.

17 K. Shanmuganathan and C. J. Ellison, Layered Double Hydroxides: An Emerging Class of Flame Retardants, in *Polymer Green Flame Retardants*, Elsevier, 2014, pp. 675–707.

18 Y. Yasin, M. N. A. Rahman, Z. Hamzah and A. Saat, Application of Response Surface Methodology for Optimization of Copper Removal from Aqueous Solution Using Magnesium Aluminum Hydrogenphosphate Layered Double Hydroxides, *Adv. Mater. Res.*, 2014, **832**, 622–627.

19 S. Daniel and S. Thomas, Layered Double Hydroxides: Fundamentals to Applications, in *Layered Double Hydroxide Polymer Nanocomposites*, Elsevier, 2020, pp. 1–76.

20 X. Guan, X. Yuan, Y. Zhao, H. Wang, H. Wang, J. Bai and Y. Li, Application of Functionalized Layered Double Hydroxides for Heavy Metal Removal: A Review, *Sci. Total Environ.*, 2022, **838**, 155693.

21 A. Zaher, M. Taha and R. K. Mahmoud, Possible Adsorption Mechanisms of the Removal of Tetracycline from Water by La-Doped Zn-Fe-Layered Double Hydroxide, *J. Mol. Liq.*, 2021, **322**, 114546.

22 R. K. Mahmoud, M. Taha, A. Zaher and R. M. Amin, Understanding the Physicochemical Properties of Zn–Fe LDH Nanostructure as Sorbent Material for Removing of Anionic and Cationic Dyes Mixture, *Sci. Rep.*, 2021, **11**(1), 1–19.

23 L. Iezzi, G. Vilardi, G. Saviano and M. Stoller, On the Equipment Design of a Spinning Disk Reactor for the Production of Novel Nano Silver in Amorphous Zeolite Particles, *Chem. Eng. J.*, 2022, **449**, 137864.

24 V. Acevedo-García, E. Rosales, A. Puga, M. Pazos and M. A. Sanromán, Synthesis and Use of Efficient Adsorbents under the Principles of Circular Economy: Waste Valorization and Electroadvanced Oxidation Process Regeneration, *Sep. Purif. Technol.*, 2020, **242**, 116796.

25 A. V. Baskar, N. Bolan, S. A. Hoang, P. Sooriyakumar, M. Kumar, L. Singh, T. Jasemizad, L. P. Padhye, G. Singh and A. Vinu, Recovery, Regeneration and Sustainable Management of Spent Adsorbents from Wastewater Treatment Streams: A Review, *Sci. Total Environ.*, 2022, **822**, 153555.

26 L. Yaqoob, T. Noor and N. Iqbal, Recent Progress in Development of Efficient Electrocatalyst for Methanol Oxidation Reaction in Direct Methanol Fuel Cell, *Int. J. Energy Res.*, 2021, **45**(5), 6550–6583.

27 V. Rives *Layered Double Hydroxides: Present and Future*; Nova Publishers, 2001.

28 Q. Wang and D. O'Hare, Recent Advances in the Synthesis and Application of Layered Double Hydroxide (LDH) Nanosheets, *Chem. Rev.*, 2012, **112**(7), 4124–4155.

29 F. Song and X. Hu, Ultrathin Cobalt–Manganese Layered Double Hydroxide Is an Efficient Oxygen Evolution Catalyst, *J. Am. Chem. Soc.*, 2014, **136**(47), 16481–16484.

30 P. A. Kobielska, A. J. Howarth, O. K. Farha and S. Nayak, Metal–Organic Frameworks for Heavy Metal Removal from Water, *Coord. Chem. Rev.*, 2018, **358**, 92–107.

31 A. A. Bakr, N. A. Sayed, T. M. Salama, I. O. Ali, R. R. A. Gayed and N. A. Negm, Kinetics and Thermodynamics of Mn (II) Removal from Aqueous Solutions onto Mg-Zn-Al LDH/Montmorillonite Nanocomposite, *Egypt. J. Pet.*, 2018, **27**(4), 1215–1220.

32 A. A. Bakr, M. S. Mostafa and E. A. Sultan, Mn (II) Removal from Aqueous Solutions by Co/Mo Layered Double Hydroxide: Kinetics and Thermodynamics, *Egypt. J. Pet.*, 2016, **25**(2), 171–181.

33 M. T. Rahman, T. Kameda, T. Miura, S. Kumagai and T. Yoshioka, Removal of Mn and Cd Contained in Mine Wastewater by Mg–Al-Layered Double Hydroxides, *J. Mater. Cycles Waste Manage.*, 2019, **21**, 1232–1241.

34 C. Modrogan, S. Căprărescu, A. M. Dăncilă, O. D. Orbuleţ, E. Vasile and V. Purcar, Mixed Oxide Layered Double Hydroxide Materials: Synthesis, Characterization and Efficient Application for Mn2+ Removal from Synthetic Wastewater, *Materials*, 2020, **13**(18), 4089.

35 E. Leiva, C. Tapia and C. Rodríguez, Removal of Mn (Ii) from Acidic Wastewaters Using Graphene Oxide–Zno Nanocomposites, *Molecules*, 2021, **26**(9), 2713.

36 O. Alagha, M. S. Manzar, M. Zubair, I. Anil, N. D. Mu'azu and A. Qureshi, Magnetic Mg-Fe/LDH Intercalated Activated Carbon Composites for Nitrate and Phosphate Removal from Wastewater: Insight into Behavior and Mechanisms, *Nanomaterials*, 2020, **10**(7), 1361.

37 H. Bolbol, M. Fekri and M. Hejazi-Mehrizi, Layered Double Hydroxide–Loaded Biochar as a Sorbent for the Removal of Aquatic Phosphorus: Behavior and Mechanism Insights, *Arabian J. Geosci.*, 2019, **12**(16), 503.

38 S. S. Alquzweeni and R. S. Alkizwini, Removal of Cadmium from Contaminated Water Using Coated Chicken Bones with Double-Layer Hydroxide (Mg/Fe-LDH), *Water*, 2020, **12**(8), 2303.

39 J. Yu, Z. Zhu, H. Zhang, Y. Qiu and D. Yin, Mg–Fe Layered Double Hydroxide Assembled on Biochar Derived from Rice Husk Ash: Facile Synthesis and Application in Efficient Removal of Heavy Metals, *Environ. Sci. Pollut. Res.*, 2018, **25**(24), 24293–24304.

40 H. Deng, S. Zhang, Q. Li, A. Li, W. Gan and L. Hu, Efficient Removal of Lead, Cadmium, and Zinc from Water and Soil by MgFe Layered Double Hydroxide: Adsorption Properties and Mechanisms, *Sustainability*, 2024, **16**(24), 11037.

41 Y. Guo, Z. Gong, C. Li, B. Gao, P. Li, X. Wang, B. Zhang and X. Li, Efficient Removal of Uranium (VI) by 3D Hierarchical Mg/Fe-LDH Supported Nanoscale Hydroxyapatite: A Synthetic Experimental and Mechanism Studies, *Chem. Eng. J.*, 2020, **392**, 123682.

42 M. B. Abd Elhaleem, A. A. Farghali, A. A. G. El-Shahawy, F. I. A. El-Ela, Z. E. Eldine and R. K. Mahmoud, Chemisorption and Sustained Release of Cefotaxime

between a Layered Double Hydroxide and Polyvinyl Alcohol Nanofibers for Enhanced Efficacy against Second Degree Burn Wound Infection, *RSC Adv.*, 2020, **10**(22), 13196–13214.

43 R. Elmoubarki, F. Z. Mahjoubi, A. Elhalil, H. Tounsadi, M. Abdennouri, M. Sadiq, S. Qourzal, A. Zouhri and N. Barka, Ni/Fe and Mg/Fe Layered Double Hydroxides and Their Calcined Derivatives: Preparation, Characterization and Application on Textile Dyes Removal, *J. Mater. Res. Technol.*, 2017, **6**(3), 271–283.

44 J. T. Kloprogge, D. Wharton, L. Hickey and R. L. Frost, Infrared and Raman Study of Interlayer Anions CO32–, NO3–, SO42–and ClO4–in Mg/Al-Hydrotalcite, *Am. Mineral.*, 2002, **87**(5–6), 623–629.

45 I. A. Ahmed, M. Badawi, A. Bonilla-Petriciolet, E. C. Lima, M. K. Seliem and M. Mobarak, Insights into the Mn (VII) and Cr (VI) Adsorption Mechanisms on Purified Diatomite/MCM-41 Composite: Experimental Study and Statistical Physics Analysis, *Front. Chem.*, 2022, **9**, 814431.

46 Y. Zeng, X. Li, Y. Chen and S. Li, High-Efficiency Adsorption of Cr (VI) and Mn (VII) from Wastewater by a Two-Dimensional Copper-Based Metal–Organic Framework, *ACS Omega*, 2023, **8**(40), 36978–36985.

47 R. M. M. dos Santos, R. G. L. Gonçalves, V. R. L. Constantino, L. M. da Costa, L. H. M. da Silva, J. Tronto and F. G. Pinto, Removal of Acid Green 68: 1 from Aqueous Solutions by Calcined and Uncalcined Layered Double Hydroxides, *Appl. Clay Sci.*, 2013, **80**, 189–195.

48 E. Scavetta, B. Ballarin, C. Corticelli, I. Gualandi, D. Tonelli, V. Prevot, C. Forano and C. Mousty, An Insight into the Electrochemical Behavior of Co/Al Layered Double Hydroxide Thin Films Prepared by Electrodeposition, *J. Power Sources*, 2012, **201**, 360–367.

49 C. Li, G. Wang, D. G. Evans and X. Duan, Incorporation of Rare-Earth Ions in Mg–Al Layered Double Hydroxides: Intercalation with an [Eu (EDTA)]– Chelate, *J. Solid State Chem.*, 2004, **177**(12), 4569–4575.

50 G. Belardi, P. Ballirano, M. Ferrini, R. Lavecchia, F. Medici, L. Piga and A. Scoppettuolo, Characterization of Spent Zinc–Carbon and Alkaline Batteries by SEM–EDS, TGA/DTA and XRPD Analysis, *Thermochim. Acta*, 2011, **526**(1–2), 169–177.

51 H. Awes, Z. Zaki, S. Abbas, H. Dessoukii, A. Zaher, A.-E. Moaty, A. Samah, N. Shehata, A. Farghali and R. K. Mahmoud, Removal of Cu2+ Metal Ions from Water Using Mg-Fe Layered Double Hydroxide and Mg-Fe LDH/5-(3-Nitrophenyllazo)-6-Aminouracil Nanocomposite for Enhancing Adsorption Properties, *Environ. Sci. Pollut. Res.*, 2021, **28**(34), 47651–47667.

52 R. Pourfaraj, S. J. Fatemi, S. Y. Kazemi and P. Biparva, Synthesis of Hexagonal Mesoporous MgAl LDH Nanoplatelets Adsorbent for the Effective Adsorption of Brilliant Yellow, *J. Colloid Interface Sci.*, 2017, **508**, 65–74.

53 M. A. Al-Ghouti and D. A. Da'ana, Guidelines for the Use and Interpretation of Adsorption Isotherm Models: A Review, *J. Hazard. Mater.*, 2020, **393**, 122383.

54 I. Langmuir, The Adsorption Of Gases On Plane Surfaces Of Glass, Mica And Platinum, *J. Am. Chem. Soc.*, 1918, **40**(9), 1361–1403, DOI: 10.1021/ja02242a004.

55 C. H. Sheindorf, M. Rebhun and M. Sheintuch, A Freundlich-Type Multicomponent Isotherm, *J. Colloid Interface Sci.*, 1981, **79**(1), 136–142.

56 J. A. A. Mead, Comparison of the Langmuir, Freundlich and Temkin Equations to Describe Phosphate Adsorption Properties of Soils, *Soil Res.*, 1981, **19**(3), 333–342.

57 M. Baudu, P. Le Cloirec and G. Martin, Pollutant Adsorption onto Activated Carbon Membranes, *Water Sci. Technol.*, 1991, **23**(7–9), 1659–1666.

58 I. Quiñones and G. Guiochon, Derivation and Application of a Jovanovic–Freundlich Isotherm Model for Single-Component Adsorption on Heterogeneous Surfaces, *J. Colloid Interface Sci.*, 1996, **183**(1), 57–67.

59 G. P. Jeppu and T. P. Clement, A Modified Langmuir-Freundlich Isotherm Model for Simulating PH-Dependent Adsorption Effects, *J. Contam. Hydrol.*, 2012, **129**, 46–53.

60 K. M. Doke and E. M. Khan, Adsorption Thermodynamics to Clean up Wastewater; Critical Review, *Rev. Environ. Sci. Bio/Technol.*, 2013, **12**(1), 25–44.

61 S. Pan, H. Shen, Q. Xu, J. Luo and M. Hu, Surface Mercapto Engineered Magnetic Fe3O4 Nanoadsorbent for the Removal of Mercury from Aqueous Solutions, *J. Colloid Interface Sci.*, 2012, **365**(1), 204–212.

62 L. del Rio, J. Åberg, R. Renner, O. Dahlsten and V. Vedral, The Thermodynamic Meaning of Negative Entropy, *Nature*, 2011, **474**(7349), 61–63.

63 M. F. R. Hanifah, J. Jaafar, M. H. D. Othman, A. F. Ismail, M. A. Rahman, N. Yusof and F. Aziz, One-Pot Synthesis of Efficient Reduced Graphene Oxide Supported Binary Pt-Pd Alloy Nanoparticles as Superior Electro-Catalyst and Its Electro-Catalytic Performance toward Methanol Electro-Oxidation Reaction in Direct Methanol Fuel Cell, *J. Alloys Compd.*, 2019, **793**, 232–246.

64 Z. X. Liang, T. S. Zhao, J. B. Xu and L. D. Zhu, Mechanism Study of the Ethanol Oxidation Reaction on Palladium in Alkaline Media, *Electrochim. Acta*, 2009, **54**(8), 2203–2208.

65 S. Gamil, W. M. A. El Rouby, M. Antuch and I. T. Zedan, Nanohybrid Layered Double Hydroxide Materials as Efficient Catalysts for Methanol Electrooxidation, *RSC Adv.*, 2019, **9**(24), 13503–13514.

66 A. Zaher, W. Kamal, D. Essam, E. M. Yousry and R. Mahmoud, Repurposing Co-Fe LDH and Co-Fe LDH/Cellulose Micro-Adsorbents for Sustainable Energy Generation in Direct Methanol Fuel Cells, *J. Water Process Eng.*, 2024, **62**, 105317.